ICAS 2021 SHANG HAI
International Council of the Aeronautical Sciences
32nd Congress of the International Council of the Aeronautical Sciences
September 6-10, 2021
Pudong Shangri-La, Shanghai, China

Experimental investigation of the hypersonic boundary layer transition on a sharp cone under different angles-of-attack

Xiwang Xu, Shihe Yi, Junhao Han, Wenpeng Zheng& Zihao Xia

College of Aeronautics and Astronautics, National University of Defense Technology, Changsha 410005, China

Abstract

The hypersonic boundary layer transition on a 7° sharp cone under different angles-of-attack (AoA) are investigated in the hypersonic quiet wind tunnel, through Nano-tracer-based Planar Laser Scattering (NPLS) techniques, high-frequency pressure sensors and temperature sensitive paints (TSP). Surface pressure measurements indicate that with the increase of the angle-of-attack, on the windward side, the second mode wave's amplitude decreases, the characteristic frequency increases, and the appearing location is rearward, and the leeward side is just the opposite. NPLS images and power spectral density (PSD) data show that when the angle-of-attack is not zero, the boundary layer transition on the centerline of the windward side is more difficult to occur. The surface temperature distribution implies that when the angle-of-attack is small (less than 7°), the transition front on the windward side moves downstream with the increase of the angle-of-attack, and the opposite is true for the leeward side. However, after the angle-of-attack reaches 7°, flow separation occurs on the leeward side, and crossflow-separation vortices and low-temperature regions appear. Notably, when AoA=10°, the windward transition front is slightly forward than when AoA=7°.

Keywords: transition, sharp cone, angle-of-attack, hypersonic boundary layer, second mode wave

1. Introduction

It is of great significance to accurately predict the occurring position of transition, which could lead to a dramatic rise in friction and heat flux on the hypersonic vehicle surface and hence affect the design of the aerodynamic layout as well as the thermal protection system of hypersonic vehicles. Wendt[1] pointed out that accurately determining the transition position of the boundary layer on the return cabin can reduce its total load by more than 20%.

The research on the boundary layer transition can be dated back to the late 19th century. Early research mainly developed from the theoretical analysis of inviscid flow to the stability analysis of viscous flow[2]. Among the results of the stability analysis, it is worth noting that Mack's conclusion. Mack[3] demonstrated the existence of the second mode wave for the first time using linear stability theory (LST). Subsequently, Demetriades[4] quantitatively confirmed the existence of the Mack second mode using hot-wire anemometry in the boundary layer on a 5° half-angle cone at Ma=8, and concluded that the second mode dominates the transition. Moreover, Demetriades[5] also observed the periodic wave structure in the laminar flow region of the boundary layer using shadow techniques in the same condition. By analyzing the wavelength and frequency of the wave structure, it is found that the formula $f \approx U_e/(2\delta)$ is satisfied, which proves that the wave structure is a second mode wave, where f is the frequency of the unstable wave, U_e is the velocity at the outer edge of the boundary layer, and δ is the thickness of the boundary layer. Stetson et al.[6, 7] investigated the stability characteristics of the sharp and blunt cone boundary layer in a conventional hypersonic wind tunnel using hot-wire anemometry at Ma=8, finding out that the pre-dominant unstable waves in the boundary layer are the second mode wave, and further verified the previous experimental results of Demetriades[4].

Cone is a classic experimental shape, and the boundary layer transition on its surface has been studied extensively. Bountin et al.[8] investigated the nonlinear processes in a hypersonic boundary layer on a sharp cone using the bicoherence method. He found that the basic mechanism of nonlinear interaction is the subharmonic resonance, and all nonlinear interactions in maximum r.m.s

voltage fluctuation are related to the second mode of disturbances. King[9] conducted a boundary layer transition study on a sharp,5° half-angle cone at various of angle-of-attack (0-4°) in a Mach (Ma) 3.5 wind tunnel, and he found that a progressive downstream and upstream motion of the transition front on the windward and leeward rays, respectively, of the cone with angle-of-attack was observed for the high noise level. Running et al.[10] studied the leeward side crossflow-induced boundary layer separation on a blunt 7° half-angle circular cone at high angle of attack using an odized-aluminum pressure-sensitive paint (AA-PSP) , and their results show that as the angle of attack increases, the separation location shift to the windward side, however, when the angle of attack is greater than or equal to 1.8× the cone's half-angle, the separation position converged to a constant azimuth angle. Marineau et al.[11, 12] investigated the influence of the angle-of-attack and the nose radii on the hypersonic boundary layer transition over the sharp and blunt cones. In their research, TSP and high-frequency pressure sensors were used to measure the transition location, and analyzed the development law of the second mode wave amplitude under different angles-of-attack(up to 6°), and they used Mack's amplitude method to predict the second mode transition. However, their research did not give the fine structure of the cone boundary layer flow field and the temperature distribution under different angles of attack, and they did not study the larger angle of attack.
Therefore, this article intends to use NPLS techniques, TSP techniques and high-frequency pressure sensors to conduct detailed experimental research on the hypersonic boundary layer transition of the sharp cone at an angle-of-attack of 0° to 10°.

2. Experimental Setup and Methods

2.1 The experimental facility

The experiments are conducted in a hypersonic quiet wind tunnel (Figure 1) at National University of Defense Technology. The design Mach number of the nozzle is 6, and its exit diameter is 300 mm. The maximum stagnation pressure and the maximum stagnation temperature is 5 MPa and 600 K, respectively. The wind tunnel can be operated at either 'quiet' or 'noisy' mode, by turning on or off the throat suction. In the quiet state, the noise level is about 0.1%[13]. A detailed description of the wind tunnel has been provided by Gang et al.[14]. The experiments are conducted at the stagnation temperature T_0=380–420 K, and stagnation pressure P_0=6–9.3 atm. The unit Reynolds number ranges from $8\times10^6\,\mathrm{m}^{-1}$ to $1.24\times10^7\,\mathrm{m}^{-1}$.

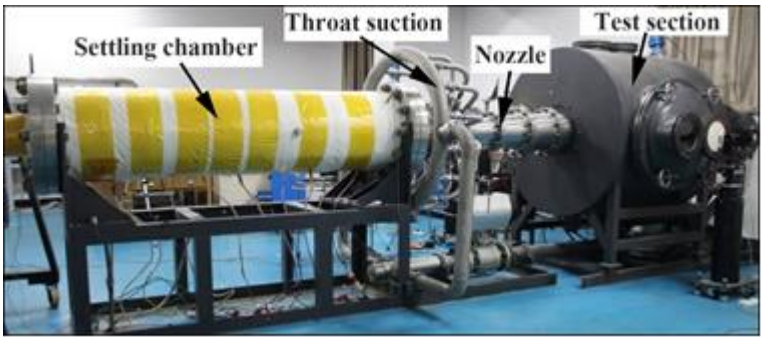

Figure 1- Hypersonic quiet wind tunnel.

2.2 The model

The experimental model is a straight cone with a 7° half-angle as shown in Figure 2. The experimental model uses the existing 7° cone model in the laboratory. The cone is divided into two sections for processing, and the nose tip can be replaced. In this experiment, a sharp nose tip with an axial length of about 145.3mm was used. The junction of the two sections is smooth, the total length of the cone is 542mm. The origin of the coordinate is located at the junction of the nose tip and body. The X-axis represents the direction of the cone generatrix, and the Y-axis normal to the wall surface. Ten PCB 132A31 high-frequency pressure (PCB) sensors are installed in the model to measure the pressure fluctuation, the coordinates are: $x_1=30$ mm , $x_2=90$ mm , $x_3=140$ mm , $x_4=180$ mm , $x_5=210$ mm , $x_6=240$ mm , $x_7=270$ mm , $x_8=300$ mm , $x_9=330$ mm , $x_{10}=360$ mm , respectively.

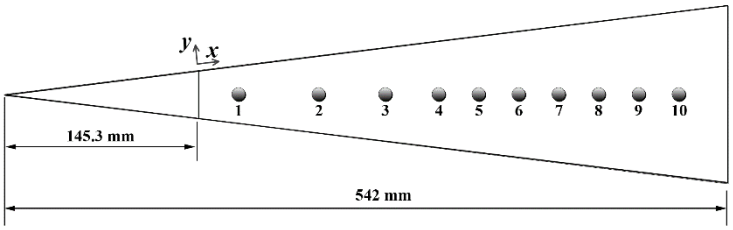

Figure 2-Schematic diagram of cone model.

2.3 Nano-tracer-based Planar Laser Scattering

Nano-tracer-based Planar Laser Scattering (NPLS) is a flow visualization techniques developed by Zhao yuxin and Yi shihe et al.[15], and its applicability for supersonic and hypersonic flow visualization has been demonstrated by many studies[16-18]. The components of NPLS system including a computer, synchronizer, CCD camera, pulsed laser, beam articulated arm, cylindrical lens, and nano-particle generator. In this study, the light source is a dual-cavity Nd: YAG laser. This laser produces laser beams with a wavelength of 532 nm, a pulse duration of 6 ns, and a maximum pulsed energy of 500 mJ. The flow is imaged using an inter-line transfer double-exposure CCD with a resolution of 2048×2048 pixels. The operating frequency of the NPLS system is 5 Hz, and the time interval between two temporal-correlated images is $5\,\mu s$.

2.4 High-frequency pressure testing techniques

The high-frequency pressure test system is mainly composed of high-frequency pressure sensors and a high-frequency data acquisition system. In this paper, the PCB 132A31 sensors (PCB sensors) is adopted for the high frequency pressure fluctuations measurement. The PCB sensor is a very high-frequency piezoelectric time-of-arrival sensor. The resonant frequency is above 1 MHz, but its performance at low frequencies is limited by a cutoff of 11 kHz. The minimum pressure resolution is 7 Pa. And the high frequency surface pressure fluctuations obtained using the PCB sensors are recorded with a DH5960 ultra high speed dynamic signal acquisition equipment. The DH5960 has 16 channels, and the sampling frequency is up to 20 MHz. The sampling frequency used in this experiment is 5 MHz.

2.5 Temperature Sensitive Paints

The TSP techniques are a measurement method to obtain the temperature distribution of the model surface through the light intensity information reflected by the temperature-sensitive fluorescent material. The temperature sensitive fluorescent material emits excitation light of a specific wavelength under the illumination of a light source. As the temperature increases, the excitation intensity of fluorescent molecules becomes weaker. By calibrating the relationship between light intensity and temperature, the temperature distribution on the model surface can be obtained. The TSP system used in this paper is composed of the TSP coating, excitation light source, CCD camera, and filter.

3. Experimental Results

3.1 NPLS Results

Figure 3 shows the streamwise NPLS image of the fine structure of the cone boundary layer at AoA=0°. The flow direction in the figure is from left to right, the range of flow visualization is x=210-400 mm, and the spatial resolution of the image is about 99.7 μm/pixel. And the unit Reynolds number of this experiment is $\mathrm{Re}=1.24\times10^{7}\,\mathrm{m}^{-1}$. Since the imaging system uses an interline transfer double-exposure CCD, two temporal-correlated NPLS images at time intervals $\Delta t=5\mu s$ could be obtained.

In Figure 3, the second mode wave with the “rope-like” structure can be observed between x =210-286mm. In the NPLS images, the second mode waves "float" at the outer edge of the boundary layer, its upper edge is in contact with the mainstream, and there is also a high-density area (close to the density of the mainstream) between the lower edge and the bottom boundary layer. In the process of moving downstream, the deformation and uplifting of the second mode waves are minute, and primarily manifest as downstream translation. Therefore, according to the pixel displacement Δx of the same structure at two moments, we can get the structure's propagation speed $U=\Delta x/\Delta t$. Meanwhile, according to the size of the pixel value of the second mode wave, its wavelength λ can be estimated. Therefore, between x =230-250mm, the average wavelength ($\overline{\lambda}$) of the second mode

wave is about 3.2mm, the average boundary layer thickness ($\overline{\delta}$) is about 1.5mm, and the average propagation velocity (U_s) is about 762m/s. Since the mainstream velocity is about 840m/s, U_s is about 0.9 times the mainstream velocity. In Figure 3, when the boundary layer develops to x =308mm, a small vortex structure begins to appear, and it gradually turns into turbulent flow.

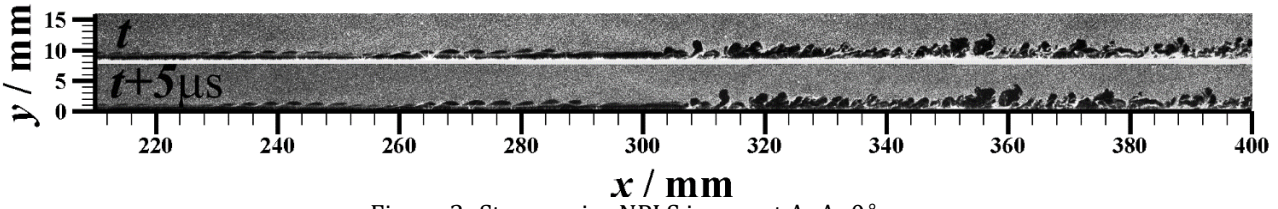

Figure 3- Streamwise NPLS image at AoA=0° .

Figure 4 and Figure 5 shows the streamwise NPLS image of the boundary layer flow on the centerline of the windward side of the cone when AoA=2° and AoA=10°, respectively. The relevant parameters of Figure 4 are the same as those of Figure 3. However, in Figure 5 the range of flow visualization is x =295-400 mm, and the spatial resolution of the image is about 51.0 μm/pixel.

Compared with Figure 3, it can be seen that under the conditions of AoA=2° and 10°, the transition of the boundary layer on the centerline of the windward side is significantly delayed. In this experiment, under the conditions of AoA=2° and 10°, there is no obvious vortex structure in the boundary layer on the center line of the windward side.

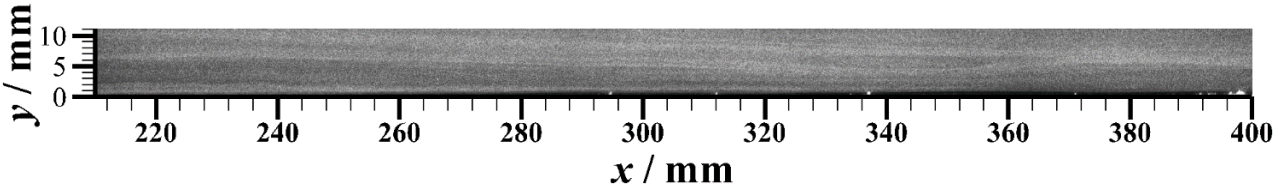

Figure 4- Streamwise NPLS image at AoA=2° .

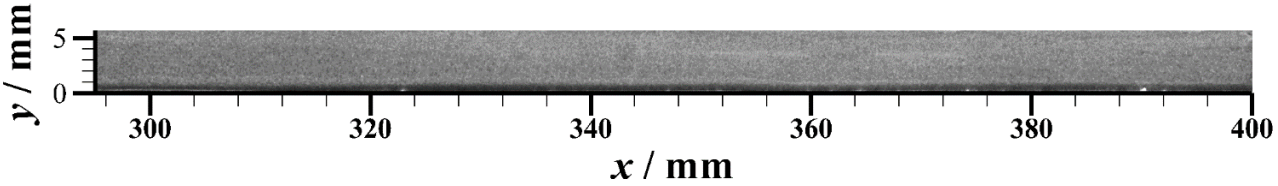

Figure 5- Streamwise NPLS image at AoA=10° .

3.2 PCB Results

Figure 6 shows the power spectral density (*PSD*) results of the pressure fluctuation at AoA=0°, 1°, 2°, and 10°. And the unit Reynolds number is $\mathrm{Re}=8.5\times10^{6}\,\mathrm{m}^{-1}$. The power spectral density (*PSD*) is calculated with Welch's method using Blackman windows with a 50% overlap and an Fast Fourier Transform (FFT) length of 2048 points. In the calculation of *PSD*, Marineau's method is adopted; i.e., the tare *PSD* (obtained before the run) is subtracted from the flow-on *PSD* to mitigate the influence of electrical noise[11]. In addition, the *PSD* curves with the angle-of-attack are the *PSD* curves of the centerline of the windward side.

Figure 6 (a) outlines the streamwise developments of the *PSD* results at AoA=0°. Between x=180-360mm, a second mode wave signal with a characteristic frequency between f=150-180kHz appears in the *PSD* curve. The second mode wave amplitude gradually increases along the flow direction between x =180-270mm. After x =270mm, the second mode wave develops into a non-linear stage, and the amplitude begins to decay gradually. And the second mode wave signal is about to disappear at x =300mm. In Figure 6 (b), when the angle-of-attack increases to 1°, a weak second mode wave appears at x =300mm and 330mm. This shows to a certain extent that when the angle-of-attack increases from 0° to 1°, the development of the boundary layer on the centerline of the windward side is delayed. In Figure 6 (c) and (d), when the angle-of-attack increases to 2° and 10°, the second mode wave signal has completely disappeared. When AoA=2°, the low-frequency components in the PSD curve at x =330 and x =360mm increase, indicating that when AoA=2°, there will be low-frequency disturbance after the boundary layer develops to x =330mm. However, when AoA=10°, even if the boundary layer develops to x =360mm, there is no obvious signal. Under this condition, the PSD curve is similar to the PSD curve of the laminar boundary layer before the second mode wave appears when AoA=0°. Therefore, the results in Figure 6 show that under these four angles-

of-attack, as the angle-of-attack increases, the development of the boundary layer is delayed.

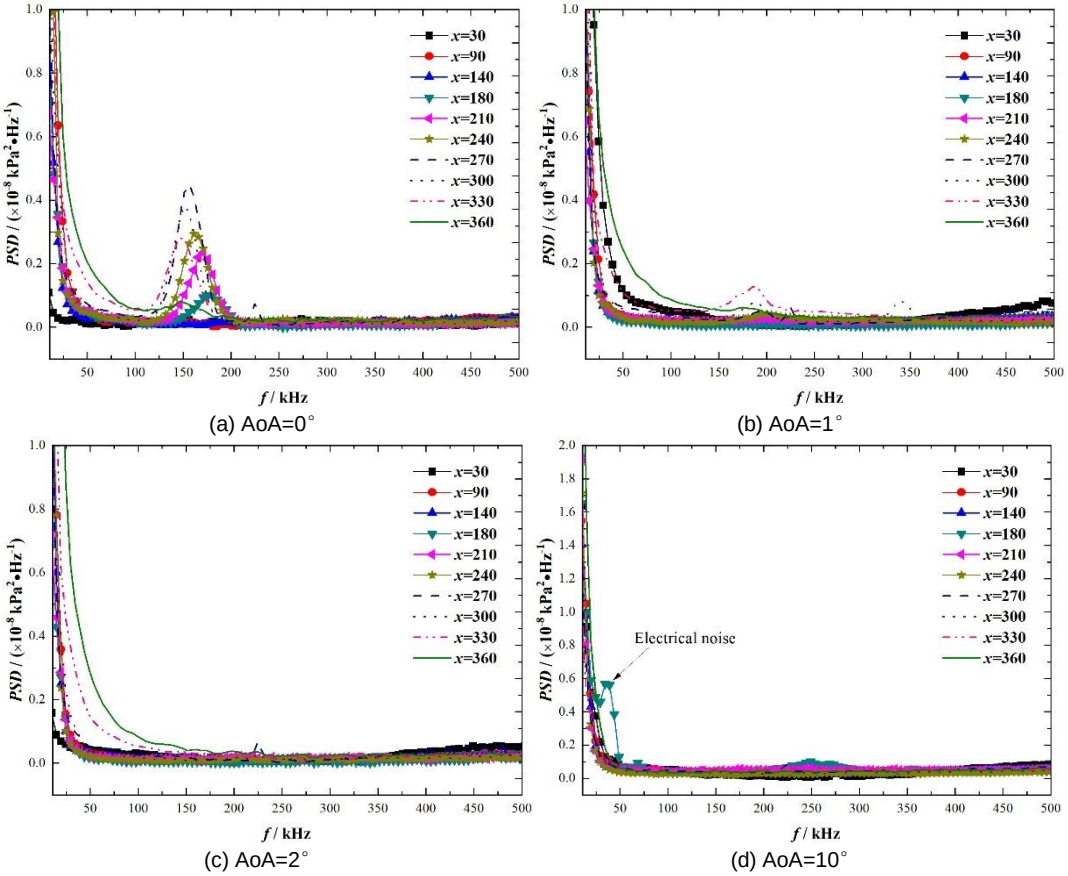

(a) AoA=0° (b) AoA=1°

(c) AoA=2° (d) AoA=10°

Figure 6- PSD results of different AoA.

Figure 7 shows the PSD distribution on the centerline of the leeward side when AoA=1°. Among them, a weak second mode wave begins to appear at x =140mm, and then the amplitude gradually increases, reaching the maximum value at x =210mm, and then the amplitude begins to attenuate. The second mode wave has disappeared at x =330mm. Compared with the result of 0° angle-of-attack in Figure 6, it can be seen that the position where the second mode wave appears, the position where it reaches the extreme value, and the position where it disappears in the boundary layer of the leeward side of the 1° angle of attack are all closer to the upstream. This indicates that the boundary layer transition on the leeward side is advanced, but the boundary layer transition on the windward side is delayed.

From the point of view of the characteristic frequency of the second mode wave, when AoA=0°, the characteristic frequencies of the second mode waves between x =180-330mm are about: 178, 171, 163, 156, 152, 148kHz (along the streamwise). When AoA=1°, the characteristic frequencies of the second mode waves between x =140-300mm on the centerline of the leeward side are approximately: 152, 144, 141, 134, 131, 128 kHz, respectively. And the characteristic frequencies of the second mode waves between x =300-330mm on the center line of the windward side are about 188 kHz and 183kHz.

Therefore, as the angle of attack increases, the characteristic frequency of the second mode wave on the leeward side decreases, while the windward side increases. This is caused by the increase in the thickness of the boundary layer on the leeward side and the decrease in the thickness of the boundary layer on the windward side.

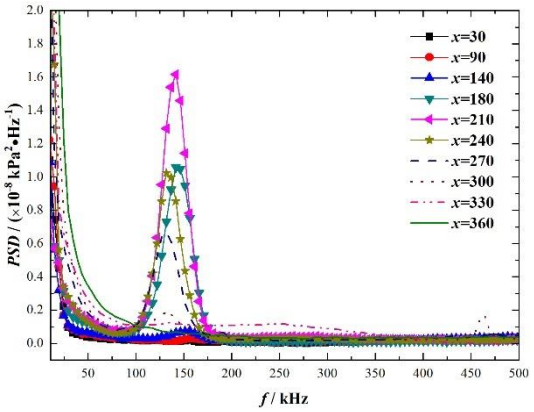

Figure 7- PSD results of 1° AoA leeward centerline.

3.3 TSP Results

The temperature rises distribution of the cone surface under different AoA are measured using TSP techniques. And the contours of the surface temperature rise for the different models are compared in Figure 8. The uppermost meridian of the cone is the centerline of the windward side, and the lowest is the centerline of the leeward side.

In Figure 8 (a), When AoA=0°, the transition location of the boundary layer on each meridian of the cone is basically the same, which is between x =340-350mm. When the angle-of-attack increases to 1° (Figure 8 (b)), the transition front of the boundary layer is tilted, and the transition location of the centerline of the windward side is postponed to after x =400mm. On the contrary, the transition location of the leeward side is shifted forward, and the transition location of the centerline of the leeward side is between x =200-210mm. When the angle-of-attack continues to increase to 2° (Figure 8 (c)), the transition front of the boundary layer is more inclined, the transition location on the windward side is more rearward, and the transition location on the leeward side is closer to the upstream.

It can be seen in Figure 8 (d) that the transition front of the boundary layer when AoA=5° is close to the transition front when AoA=2°. However, there are some heat flux bands on the leeward side when AoA=5°. These bands indicate that when AoA=5°, the cross flow in the boundary layer has developed more obviously. However, when the angle-of-attack increases to 7°, as shown in Figure 8 (e), the transition front of the boundary layer is different from the transition front under the condition of a small angle-of-attack. Under this condition, the transition front of the boundary layer on the windward side is similar to the transition front under the small angle-of-attack, and both closer to the centerline of the windward side, the more backward the transition position of the boundary layer is. It is worth noting that when AoA=7°, the heat flux band is more obvious, and the transition front on the leeward side has gradually disappeared and replaced by a large number of heat flux bands. This is caused by the formation of a detachment vortex when the crossflow vortex on the leeward side is rolled up when AoA=7°.

In Figure 8 (f), after the angle-of-attack increases to 10°, the temperature rise on the windward side increases significantly, and the boundary layer transition front moves slightly forward compared to the boundary layer transition at AoA=7°. However, compared with the transition when AoA=0°, it is still delayed. At the same time, the boundary layer separation on the leeward side is more serious, and in the measurement range, the leeward side is mostly some heat flux bands, which formed by the crossflow-separation vortices. Moreover, due to the rolling up of the crossflow-separation vortices, a large number of low temperature areas appear on the leeward side.

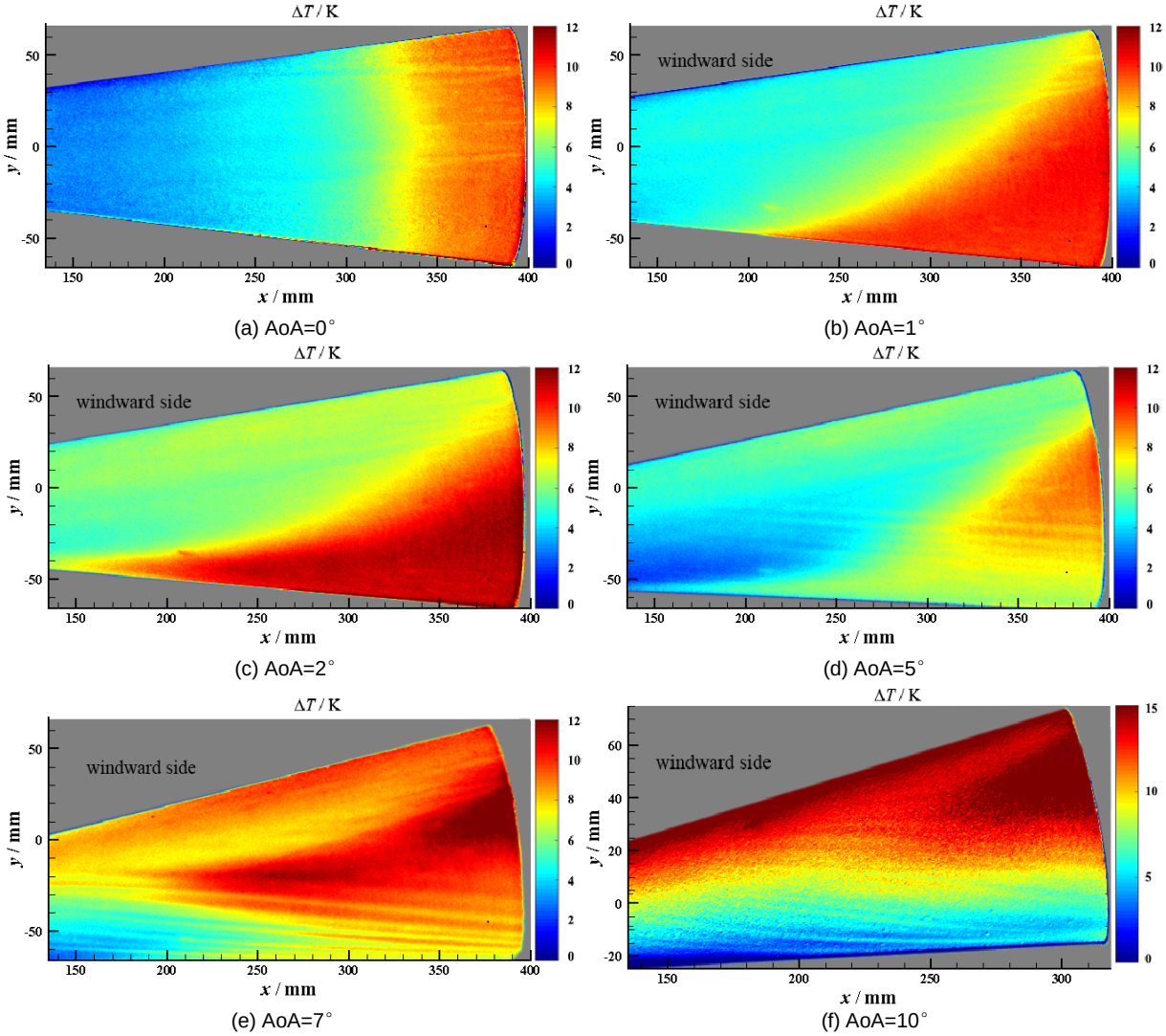

Figure 8- TSP results of different AoA.

4. Summary and conclusions

In this paper, the hypersonic boundary layer transition on a sharp straight cone at AoA=0°, 1°, 2°, 5°, 7°, and 10° is investigated in a Ma 6 wind tunnel using the NPLS techniques, PCB sensors, and TSP techniques. With detailed comparisons of the experimental results, some meaningful conclusions have been obtained as shown below.

(1) At 0° angle-of-attack and small angle-of-attack (AoA=1°,in this paper), the second mode instability dominates during the transition of the sharp cone boundary layer. With the increase of the angle-of-attack, the second mode wave's amplitude on the windward side decreases, the characteristic frequency increases, and the appearing location is rearward, and the leeward side is just the opposite.

(2) After the angle-of-attack increased to 5°, the crossflow mode in the boundary layer of the leeward side of the sharp cone gradually became dominant. The transition front of the boundary layer on the windward side is similar to that under the condition of a small angle-of-attack. However, the situation on the leeward side is more complicated: when the boundary layer on the leeward side is not separated and the crossflow-separation vortices are not rolled up, the transition front of the boundary layer on the leeward side is similar to the transition front at a small angle-of-attack; when the angle-of-attack continues to increase (AoA≥ 7° in this paper), the leeward side will roll up the crossflow-separation vortices, separate the boundary layer, a large number of heat flow bands will appear, and some low temperature regions will appear.

(3) When the angle-of-attack is less than 7° (half cone angle), the transition front of the boundary layer on the windward side of the sharp cone moves downstream with the increase of the angle-of-attack, and the opposite is true for the leeward side.

(4) Compared with the results of the 7° angle-of-attack and the 10° angle-of-attack, when AoA=10°, the boundary layer transition front on the windward side moves forward, and the range of the

separation vortices (or the separation zone and the low temperature area) on the leeward side is also larger.

5. Copyright Issues

References

[1] Wendt, J.F. External hypersonic aerodynamics: State-of-the-art and future perspective. In: AGARD Conference Proceedings AGARD CP, AGARD, 1997, Vol. 3, pp. C10-C10.

[2] Liu X, Lai G, Wu J. Boundary-layer transition experiments in hypersonic flow. Acta Aerodynamica Sinica. 2018;36(02):196-212[Chinese].

[3] Mack L. Linear stability theory and the problem of supersonic boundary-layer transition. AIAA Journal. 1975;13(3):278-289.

[4] Demetriades A. Hypersonic viscous flow over a slender cone. III-Laminar instability and transition. Proceedings of the 7th Fluid and Plasma Dynamics Conference, 1974.

[5] Demetriades A. Boundary-layer instability observations at Mach number 7. Journal of Applied Mechanics 1977;44(1):7.

[6] Stetson K, Thompson E, Donaldson J, et al. Laminar boundary layer stability experiments on a cone at Mach 8. I-Sharp cone. AIAA-83-1761. Reston:AIAA,1983.

[7] Stetson K, Thompson E, Donaldson JC, et al. Laminar boundary layer stability experiments on a cone at Mach 8. II- Blunt cone. AIAA-84-0006. Reston:AIAA,1984.

[8] Bountin D, Shiplyuk A, Maslov A. Evolution of nonlinear processes in a hypersonic boundary layer on a sharp cone. Journal of Fluid Mechanics. 2008, 611, pp. 427-442.

[9] King R. Mach 3.5 boundary-layer transition on a cone at angle of attack. 1991.

[10]Running, C.L., Sakaue, H., Juliano, T.J. Hypersonic boundary-layer separation detection with pressure-sensitive paint for a cone at high angle of attack. Experiments in Fluids. 2019, 60, p. 13.

[11]Marineau E, Moraru G, Lewis DR, et al. Mach 10 Boundary Layer Transition Experiments on Sharp and Blunted Cones*. Proceedings of the AIAA International Space Planes & Hypersonic Systems & Technologies Conference*, 2014.

[12]Marineau EC, Moraru GC, Lewis DR, et al. Investigation of Mach 10 Boundary Layer Stability of Sharp Cones at Angle-of-Attack, Part 1: Experiments. Proceedings of the AIAA Aerospace Sciences Meeting, 2015.

[13] Yi S, Liu X, Lu X, et al. Application of NPLS technique in the researches on hypersonic boundary layer transition. Acta Aerodynamica Sinica. 2020;38(2):348-354.

[14] Gang D, Yi S, Lu X. Design and performance of a hypersonic quiet wind tunnel at NUDT. Proceedings of the 21st AIAA International Space Planes and Hypersonic Technologies Conference, 2017.

[15] Zhao Y, Yi S, Tian L, et al. Supersonic flow imaging via nanoparticles. Science in China. 2009;52(12):3640-3648.

[16] Xu X, Yi S, Zhang F, et al. Influences of Steps on the Hypersonic Boundary-Layer Transition on a Cone[J]. AIAA Journal, 2021, 59(2):439-446.

[17] Zhang F, Yi S, Xu X, et al. A swept fin-induced flow field with different height mounting gaps. Chinese Journal of Aeronautics. 2021, 34, pp. 148-162.

[18] Liu X, Yi S, Niu H, et al. Experimental investigation about the second-mode waves in hypersonic boundary layer over a cone at small angle of attack. Experimental Thermal and Fluid Science, 2020; 118: 8.